Corrosion Science 164 (2020) 108345

Contents lists available at ScienceDirect

Corrosion Science

journal homepage: www.elsevier.com/locate/corsci

Dual role of nanosized NbC precipitates in hydrogen embrittlement susceptibility of lath martensitic steel

Shiqi Zhang[a,b], Jifang Wan[c], Qiyue Zhao[a], Jing Liu[d], Feng Huang[d], Yunhua Huang[a,*], Xiaogang Li[a,*]

[a] Corrosion and Protection Center, University of Science and Technology Beijing, Beijing 100083, China
[b] Key Laboratory of Advanced Materials (MOE), School of Materials Science and Engineering, Tsinghua University, Beijing 100084, China
[c] Research Institute of Petroleum Exploration and Development, Beijing 100083, China
[d] The State Key Laboratory of Refractories and Metallurgy, Wuhan University of Science and Technology, Wuhan, Hubei 430081, China

ARTICLE INFO

Keywords:
A. Hydrogen embrittlement
B. Hydrogen diffusion
C. NbC precipitate
D. Martensitic steel

ABSTRACT

The effect of dispersed nanosized spherical NbC precipitates (~10 nm) on the hydrogen embrittlement (HE) of martensitic steel was investigated by slow strain rate tests, hydrogen permeation tests, atom probe tomography and microstructural examination. HE susceptibility decreases as the amount of NbC increases. NbC plays dual roles in HE. Primarily, NbC alleviates hydrogen accumulation in other areas via hydrogen traps which are induced by NbC directly and increased by the additional grain boundaries resulting from NbC, inhibiting the hydrogen-enhanced decohesion. Moreover, NbC impedes the hydrogen-enhanced localized plasticity by pinning hydrogen-dislocation atmospheres and reducing Σ3 boundary fraction. Secondarily, NbC weakens the beneficial {111}//ND texture, reduces the crack-propagation resistance, and plays a harmful role.

1. Introduction

High-strength martensitic steels are widely used for structural components in various industries, such as aircraft, automobiles, and tools. However, one of the significant challenges limiting the application of ultrahigh-strength martensitic steel is hydrogen embrittlement (HE), as the martensite microstructure is highly susceptible to HE and the susceptibility of steels to HE increases with the strength [1–6]. During the manufacturing and service process, e.g. smelting, acid pickling, welding, and exposure to corrosive environments, hydrogen atoms easily diffuse into martensitic steel, degrading the mechanical properties [7–9]. Owing to the detrimental impact of hydrogen on high-strength steels, numerous studies have been performed on the HE behavior [10–19]. The prevalent mechanisms include internal pressure theory [12], hydrogen-enhanced decohesion (HEDE) [13,14], hydrogen-enhanced vacancy stabilization [15], hydrogen-enhanced localized plasticity (HELP) [16,17], and adsorption-induced dislocation emission [18]. In particular, in the case of lath martensitic steel, HE fracture generally results from a combination of HELP and HEDE, and the local hydrogen concentration determines the dominant HE mechanism [19–21].

Strategies for enhancing the HE resistance of steels have been extensively investigated. Various methods have been employed, e.g. controlling the inclusion size and amount [22], decreasing the chemical composition segregation [23], grain-boundary engineering [24], introducing effective hydrogen traps [25,26], adding microalloying elements [27–35] and texture engineering [36–38]. One of the most promising methods is generating precipitates by adding carbide formers, such as V, Ti, and Nb, to steel. It has been well established that these carbides (VC, TiC, NbC) reduce the HE susceptibility by introducing effective hydrogen traps; moreover, they induce precipitation strengthening, improving the strength of steels [30,33,34]. For example, Kim et al. [30] and Depover et al. [31] found that the HE resistance of martensitic steel and Fe-C-Ti alloys, respectively, were enhanced by TiC precipitates. Lee et al. [32] and Cho et al. [33] reported that the precipitation of V carbide in V-bearing martensitic steels reduced the HE susceptibilities. Lin et al. [35] found that the presence of Nb (C, N) precipitates was beneficial to the HE resistance of press-hardened steel owing to its hydrogen-trapping role.

To prove the hydrogen-trapping role of carbides, numerous experimental studies have been performed. Wei et al. [39] investigated the hydrogen-trapping capacity of TiC, VC, and NbC via thermal desorption spectroscopy (TDS) and reported that NbC had the largest trapping capacity. In other studies, Wei et al. [40,41] found that coherent or semi-coherent carbides could trap H at room temperature, whereas the incoherent TiC could only trap hydrogen at elevated

* Corresponding authors.
E-mail addresses: huangyh@mater.ustb.edu.cn (Y. Huang), lixiaogang99@263.net (X. Li).

https://doi.org/10.1016/j.corsci.2019.108345
Received 18 July 2019; Received in revised form 26 October 2019; Accepted 12 November 2019
Available online 14 November 2019
0010-938X/

temperatures. Turk et al. [42] examined the hydrogen-trapping capacity of VC with different sizes and concluded that nano sized carbides are found to trap more hydrogen, with optimal size typically around 10 nm. Moreover, direct observations of hydrogen-trapping sites in precipitates of micro-alloyed steels have been achieved recently via atom probe tomography (APT) on hydrogen/deuterium charged samples [3,43–49]. Takahashi et al. [43] found that C vacancies on the (001) broad surface of fine TiC and V_4C_3 were the main hydrogen-trapping sites. Chen et al. [45] found that deuterium atoms were trapped in the core of V-Mo-Nb carbides through composition profile analysis via APT on the deuterium charged samples. The reason for selection of deuterium charging rather than hydrogen charging in their work is that the residual hydrogen gas in the chamber can be absorbed on the sample and also be mapped by APT. Thus, the hydrogen concentration obtained by APT on hydrogen charged sample contain background hydrogen and could only be used for qualitative analysis [46–49]. In contrast, the APT test on deuterium charged sample can remove the influence of hydrogen gas in chamber and only measure the deuterium in the material, and thus can be used for quantitative analysis [46].

Although the hydrogen-trapping capacity of carbides and the beneficial effects of V and Ti carbides on the HE behavior have been widely reported [29–33,39–41], the effects of NbC precipitates on the hydrogen-trapping sites and HE in steels lack adequate research and are not fully understood. In particular, although the hydrogen-trapping role of NbC precipitates has been proven via TDS [39,50], the trapping of hydrogen atoms in NbC precipitates has not been directly observed via APT. Moreover, although the quantitative estimation of the density of hydrogen traps induced directly by NbC precipitate has been achieved using thermokinetic simulation approach [51], the density of other types of traps, such as traps related to dislocation, martensite packets, block and lath boundaries which were influenced by NbC precipitates, has not been achieved. The effects of these carbides on HE are generally attributed to their strong hydrogen-trapping capacity [29–35]. However, these carbides may also significantly change the microstructure, and the influence of the microstructure change on the HE are often ignored and are not fully understood.

Therefore, the objective of this study was to elucidate the effect of NbC precipitates on the HE behavior of lath martensitic steel. Three steels with different NbC amounts were prepared. The precipitates in the steels were examined via transmission electron microscopy (TEM). The HE susceptibilities of the steels were evaluated via slow strain rate tests (SSRTs) of hydrogen pre-charged specimens. The features of the fracture surfaces, crack-propagation paths, and failure mechanisms were investigated via a combination of field-emission scanning electron microscopy (FESEM), high-angular resolution electron backscatter diffraction (HAR-EBSD), and electron channelling contrast imaging (ECCI). The hydrogen-diffusion behavior was examined and the hydrogen-trapping sites in the steels were directly observed via hydrogen permeation tests and APT. According to the microstructure features, a quantitative model was established and used to evaluate the density of each type of trap. Additionally, the crystallographic characteristics of the cross section underneath the fracture surface in different hydrogen-charged specimens were observed via EBSD. Finally, the effect of the NbC precipitates on the HE resistance of the lath martensitic steel was discussed according to the changes in the microstructure and hydrogen traps.

2. Materials and methods

2.1. Materials

Low-carbon lath martensitic steels with different Nb contents were used in this study, and their detailed chemical compositions are presented in Table 1. The N1 steel was a Nb-free steel. To obtain different amounts of NbC precipitates, 0.021 and 0.055 wt.% Nb were added for the N2 and N3 steels, respectively. The other chemical elements had similar contents in these steels. The casting laboratory-scale ingots were prepared and homogenized at 1230 °C for 60 min, followed by a hot-rolling process. The finish rolling temperature was about 850 °C, and the final thickness was about 3.5 mm, then the steel sheet was cooled down to room temperature in the furnace. Subsequently, these plates were subjected to the same heat-treatment process. All the plates were reheated to 930 °C for 3 min and quenched in water.

Table 1
Chemical compositions of the experimental martensitic steels (wt.%).

Steel	C	Mn	Si	Al	Cr	B	Nb	P	S	Fe
N1	0.235	1.19	0.31	0.041	0.166	0.0022	0	0.008	0.005	Val.
N2	0.236	1.20	0.32	0.042	0.165	0.0023	0.021	0.009	0.004	Val.
N3	0.234	1.21	0.32	0.040	0.168	0.0022	0.055	0.008	0.005	Val.

2.2. HE susceptibility tests

The HE susceptibilities of the tested steels were evaluated via SSRT tests with a strain rate of 6.6×10^{-5} s^{-1} at room temperature. According to ASTM E8 M, smooth specimens with a gauge dimensions of 25 (length) × 6 (width) × 1.5 (thickness) mm^3 were cut from the steel sheets and ground with SiC paper (up to 2000 grit). The length and width direction are the rolling direction (RD) and transverse direction (TD) of the hot-rolled steel, respectively. Then, the specimens were divided into two groups. The specimens in the first group were electrochemically hydrogen-charged in a solution of 0.5 mol/L H_2SO_4 and 0.25 g/L thiourea at 0.5 mA/cm^2 for 1 h, followed by tensile-strain tests. The specimens in the other group were tensile-deformed without H pre-charging. After the tests, the HE-susceptibility index (I_{HE}) of each steel was calculated as follows:

$$I_{HE} = \frac{\delta_0 - \delta_H}{\delta_0} \times 100\% \quad (1)$$

Where, δ_0 and δ_H represent the tensile elongations of specimens with and without H pre-charging, respectively.

2.3. Microstructure and fractography feature observations

To examine the microstructure and prior austenite grain (PAG) of the experimental steels, samples were cut from each steel plate and then ground using SiC paper, followed by polishing with 1-μm diamond paste. Finally, the samples were etched with a 4% Nital solution and a saturated aqueous picric acid solution and then observed via TESCAN MIRA3 FESEM and optical microscopy (OM, Olympus BC51 M). Precipitate observation was performed for all the samples via TEM (Tecnai F30) at 200 kV. The foils for TEM were ground to approximately 80 μm and then electropolished with 10% perchloric acid and 90% ethanol using a twin-jet electropolishing device at a low temperature. The phase compositions and dislocation densities of the materials were examined via X-ray diffraction (XRD) analysis with Cu K_α radiation, and the step size was 0.02°. Prior to the XRD measurements, the surfaces of samples (RD-TD planes) were prepared via electropolishing to remove the stress layer, and after the tests, the modified Williamson–Hall method was used to calculate the dislocation density [52].

The fracture surfaces of hydrogen-charged and hydrogen-free specimens after the SSRT were examined via FESEM. To elucidate the HE mechanism of the tested martensitic steel, the hydrogen-assisted cracks in the region near the fracture surface (the detailed location is shown in the blue box of Fig. 1 and the examination plane is RD-TD plane) of the N1 steel were carefully examined via SEM, ECCI, and HAR-EBSD. The HAR-EBSD measurements were performed using a TESCAN MIRA3 FESEM with an Oxford Symmetry EBSD detector, which is a

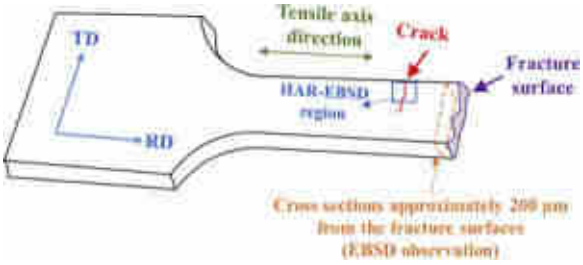

Fig. 1. Schematic of the crack position and the cross-section position.

complementary metal–oxide semiconductor-based detector that provides an angle resolution of approximately 0.05°–0.1°. To reveal the dislocation structures, a step size of 100 nm and the resolution (no binning) mode were selected. Moreover, EBSD measurements were performed to examine the crystallographic characteristics of the cross sections below the fracture surfaces (Fig. 1) of the hydrogen-charged specimens. All the samples for the EBSD measurements were mechanically polished using 1-μm diamond paste and then vibration-polished in a 0.05-μm colloidal silica slurry for 8 h.

2.4. Hydrogen permeation test

To evaluate the status of the hydrogen traps in the steels, hydrogen permeation tests were performed on all the steels using a Devanathan–Stachurski dual cell [53] at room temperature. The reference electrode and counter electrode were a saturated calomel electrode and Pt, respectively. Samples with dimensions of $20 \times 20 \times 1.2$ mm^3 were machined and ground to a thickness of approximately 1 mm, followed by mechanical polishing to remove the flux-limiting surface impedances. Because an oxide layer may have been formed on the hydrogen-discharging sides of the samples during hydrogen permeation, in the final step of sample preparation, the hydrogen-discharging sides were electroplated with Ni. After the samples were mounted between the charging cell and oxidation cell, a 0.2 M NaOH solution was poured into the oxidation cell, and a constant potential of 250 mV_{SCE} was applied on the oxidation side using an electrochemical workstation. When the oxidation current density decreased to < 0.5 μA/cm^2, 0.5 mol/L H_2SO_4 + 0.25 g/L thiourea was poured into the hydrogen-charging cell, and the hydrogen-charging side of the sample was electrochemically charged. Once the oxidation current was stabilized, the hydrogen charging was interrupted, and the hydrogen permeation was completed. Then, the permeation parameters, i.e. the effective hydrogen diffusivity (D_{ap}) and diffusion hydrogen concentration (C_0), were calculated using the following equations [54,55]:

$$J_\infty L = \frac{I_\infty L}{FS} \tag{2}$$

$$C_0 = \frac{J_\infty L}{D_{ap}} \tag{3}$$

$$D_{ap} = \frac{L^2}{6t_{0.63}} \tag{4}$$

Where, L represents the specimen thickness, I_∞ represents the steady-state current density, J_∞ represents the hydrogen flux, F represents the Faraday constant, $t_{0.63}$ represents the time lag for the current density to reach $0.63I_\infty$, and S represents the exposure area during permeation (1.76 cm^2).

2.5. Observation of hydrogen-trapping sites via APT

Direct observation of hydrogen-trapping sites in the Nb-bearing steel was achieved via APT using a CAMECA LEAP 4000X HR. A square

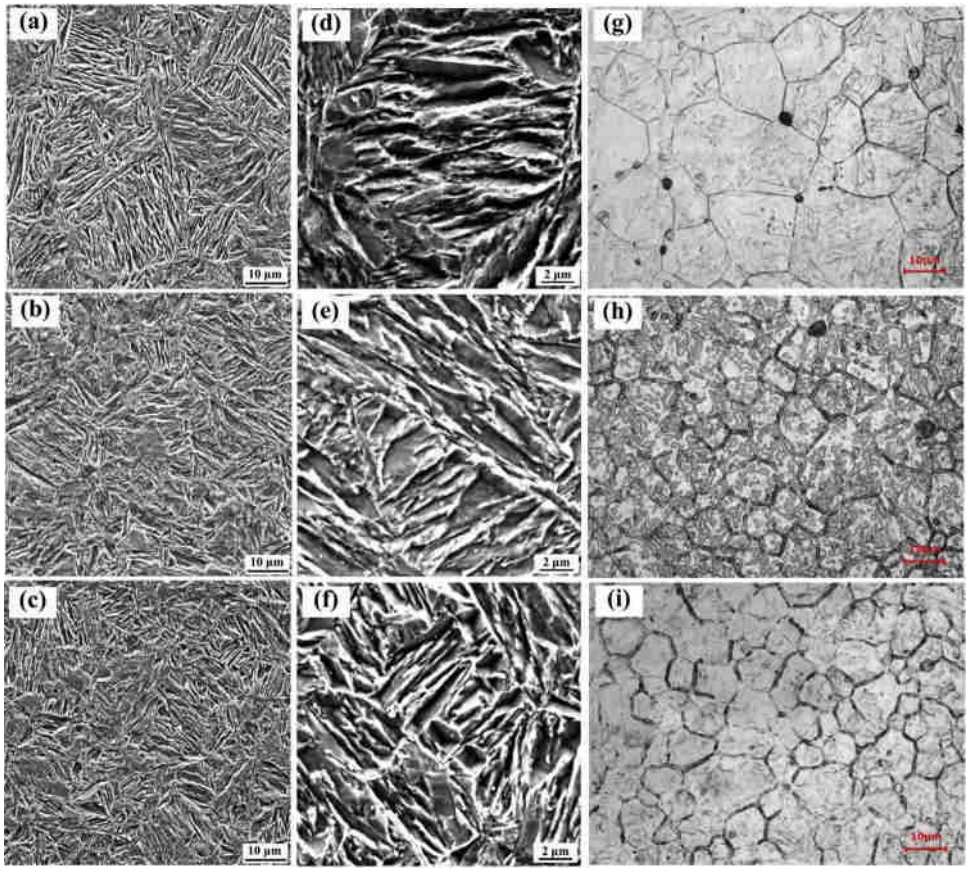

Fig. 2. Low- and high-magnification SEM micrographs of the microstructures of (a, d) N1, (b, e) N2, and (c, f) N3; PAG morphologies for (g) N1, (h) N2, and (i) N3.

rod with dimensions of approximately 0.5 × 0.5 × 20 mm^3 was cut from the N3 steel and ground using SiC paper. Then, it was electropolished to obtain a needle-like specimen. As hydrogen could be introduced by the electropolishing, similar to previous studies [46–48], additional electrochemical charging was not applied to the specimen during the sample preparation. After the electropolishing, the specimen was immediately placed into the chamber, and APT analyses were conducted at a tip temperature of 60–100 K under ultrahigh vacuum with a pulse fraction of 0.2 and a pulse repetition rate of 2 kHz. The raw data were analysed using the IVAS™ software.

3. Results and discussion

3.1. Microstructural characterizations

Fig. 2a–f show SEM images of the microstructures of the investigated steels. All the steels exhibited a fully lath martensite microstructure, with the PAG composed of a martensite hierarchical structure, i.e. laths, blocks, and packets. With the increasing Nb content, the martensite microstructure (Fig. 2a–f) became finer and more homogeneous, and the PAG size (Fig. 2g–i) decreased. This is because the presence of NbC precipitates in Nb-bearing steel can inhibit the austenite grain growth at high temperatures [56]. Additionally, as indicated by the XRD results in Fig. 3, all the steels consisted of a fully body-centred cubic (bcc) iron phase without a retained austenite phase.

Fig. 4 shows TEM images of the precipitates in the tested steels. In the N1 steel (Fig. 4a), several parallel martensite laths (but no precipitates) were observed. In the N2 and N3 steels, numerous dispersed nanosized precipitates were observed, and the volume fraction of NbC precipitate increases with increasing Nb content. Both the precipitates in N2 and N3 are approximately spherical and distributed uniformly in the matrix. Moreover, the average precipitate size was similar (average diameter of ~10 nm, ranging from 4–30 nm) between these two Nb-bearing steels, but the amount of precipitates in the higher-Nb content steel (N3) was significantly larger than that in the lower-Nb content steel (N2). To confirm the precipitate type, energy-dispersive X-ray spectroscopy (EDS) and selective-area diffraction (SAD) were conducted on the precipitates, and the results indicated that these precipitates were face-centred cubic (fcc) NbC. Examples of the EDS and SAD results for the precipitate in Fig. 4c are shown in Fig. 4d and e, respectively. Moreover, in high-magnification TEM micrographs of the Nb-bearing steels, as shown in f, dislocations were observed to be pinned by part of the NbC precipitates.

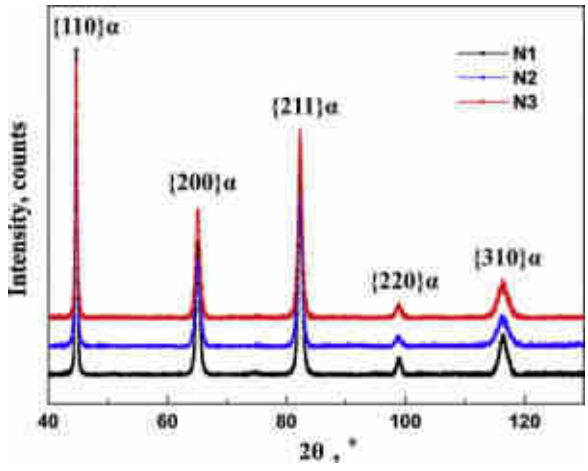

Fig. 3. XRD patterns of experimental steels with different Nb contents.

3.2. Mechanical properties

The microstructural observation clearly shown that these steels contain different amount of NbC precipitates. To study the influence of NbC precipitates on the HE susceptibilities of the tested lath martensitic steels, the hydrogen-uncharged and hydrogen-charged tensile specimens from these three steels were subjected to SSRT tests. To ensure the reliability of the experimental data, the SSRT tests were repeated three times on each steel, and only the curves with mechanical properties closest to the average values were presented. The engineering stress–-strain curves of hydrogen-uncharged and hydrogen-charged samples with different NbC precipitate amounts are shown in Fig. 5, and the corresponding mechanical data are presented in Table 2. The mechanical properties of the three hydrogen-uncharged specimens exhibited slight differences, whereas those of the three hydrogen-charged specimens differed significantly. The tensile strength and elongation of the hydrogen-uncharged steels increased slowly with an increase in the NbC amount, owing to the precipitate strengthening and refinement strengthening of the NbC precipitates [57]. In contrast, the elongation of the hydrogen-charged samples increased significantly with the increasing NbC amount, from 2.3%–5.7%. And the tensile strength of hydrogen-charged samples was also increased after adding different amount of NbC. Additionally, with an increase in the NbC amount, the HE index decreased significantly (from 72.6%–35.9%), indicating that the NbC precipitates improved the HE resistance of the experimental martensitic steel.

3.3. Fractography characterization

As shown in Fig. 6, the fracture surfaces of all the specimens without hydrogen exhibited the ductile fracture mode, with typical dimple morphologies. In contrast, as shown in Fig. 7, the fracture surfaces of the different hydrogen-charged specimens exhibited significant differences. In the N1 steel (Fig. 7a), most regions exhibited a mixed mode of intergranular (IG) and quasi-cleavage (QC) fracture, while a small region of the surface exhibited QC fracture. In the IG + QC mixed fracture region (Fig. 7b), several smooth facets and secondary cracks that propagated along the PAG boundaries were observed, indicating that IG fracture occurred in this region. Additionally, characteristics of QC fracture, such as serrated markings and lath-like features, were also observed in this region. These lath-like features had similar dimensions to the martensite lath, indicating that the fracture path for this region was along the lath boundaries. In the QC region (Fig. 7c), many fine tear ridges were observed. The existence of fine tear ridges and serrated markings indicated that the plastic process was an integral part of the hydrogen-assisted cracking in the experimental steels [21,58,59].

Moreover, as shown in Figs. 7a, d, and g, with the increasing NbC precipitate amount, the fraction of ductile regions increased. Specifically, the fracture of N2 steel was a mixed fracture of IG + QC, ductile microvoid coalescence (MVC) + QC, and MVC. In the MVC + QC region (Fig. 7e) of the N2 steel, in addition to serrated markings and lath-like features, several large tearing ridges appeared, indicating that this region was subjected to a more significant plastic deformation [60]. The morphologies of the IG + QC zone (Fig. 7f) in N2 were similar to those for N1 (Fig. 7b). Furthermore, N3 exhibited a mixture feature of MVC + QC (Fig. 7h), IG + QC, and MVC (Fig. 7i), and MVC was the primary mode.

3.4. Hydrogen-assisted cracking characteristics and mechanism

Previous studies [20,58,61,62] suggested that IG fracture is evidence of the HEDE mechanism, and local ductile features (such as fine tear ridges and serrated markings) are evidence of the HELP mechanism. The coexistence of IG + QC fracture in the N1 steel indicated the HE mechanism possibly the combination of HEDE and HELP. To directly elucidate the HE mechanism and cracking characteristics of the

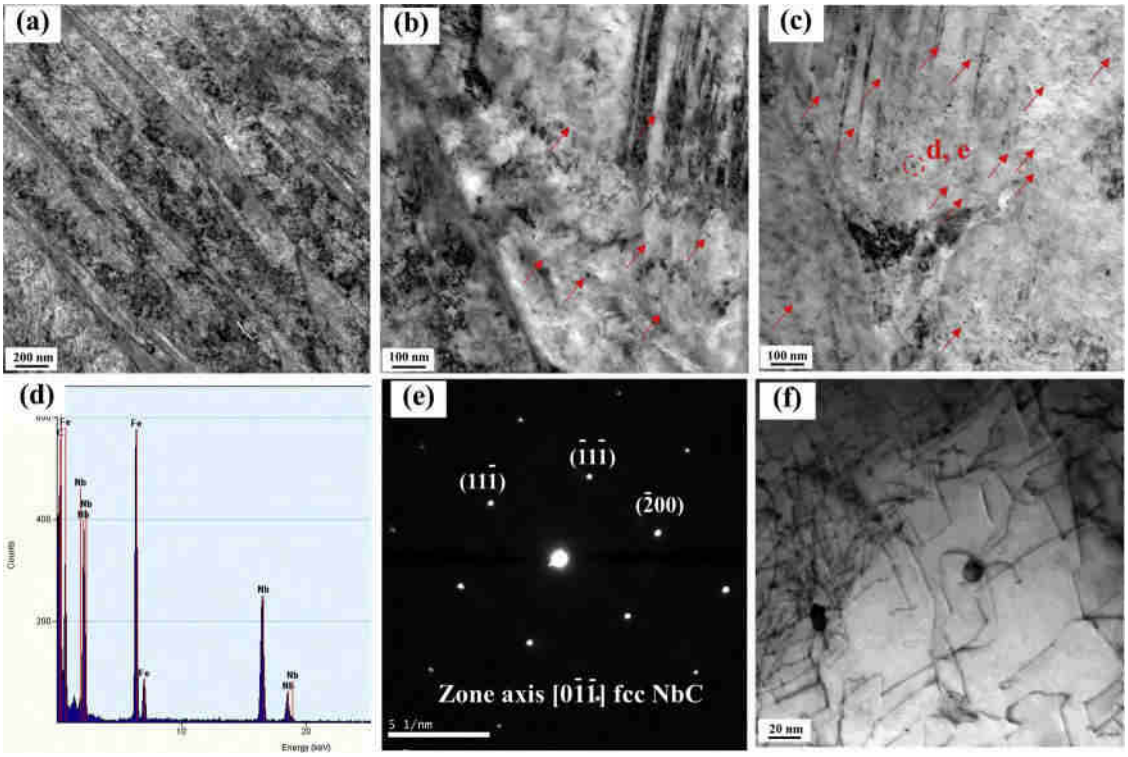

Fig. 4. TEM images showing the morphologies of the precipitates in (a) N1, (b) N2, and (c) N3. (d) EDS and (e) SAD results for the precipitate indicated by the red circle in N3. Part of the nanosized precipitates is marked by red arrows in (b) and (c). (f) High-magnification TEM micrograph of the precipitates in N3. (For interpretation of the references to colour in this figure legend, the reader is referred to the web version of this article).

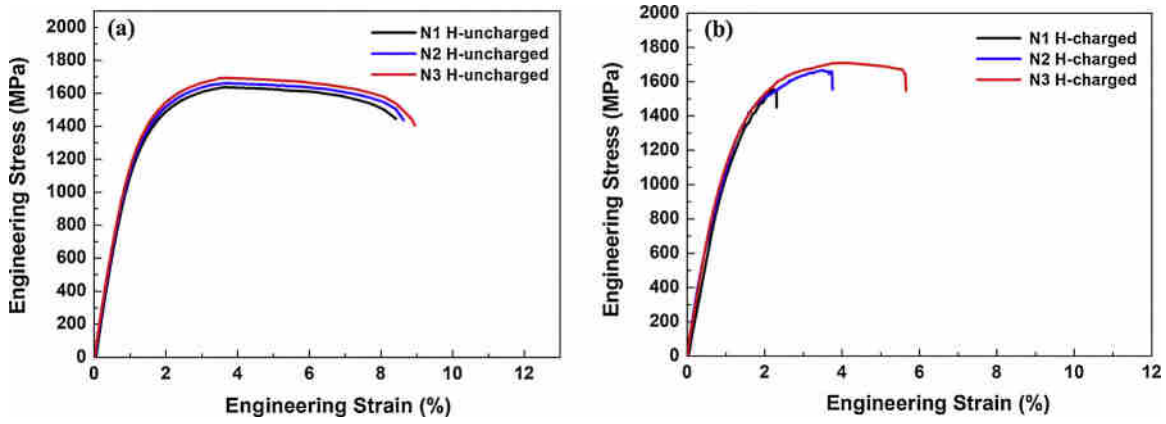

Fig. 5. Engineering stress–strain curves of the (a) hydrogen-uncharged and (b) hydrogen-charged specimens.

Table 2
Mechanical properties of the hydrogen-uncharged and hydrogen-charged experimental steels.

	N1		N2		N3	
	H-free	H-charged	H-free	H-charged	H-free	H-charged
Tensile strength (MPa)	1637	1550	1663	1664	1693	1697
Yield strength (MPa)	1019	1008	1077	1069	1123	1125
Elongation (%)	8.4	2.3	8.6	3.8	8.9	5.7
I_{HE} (%)	72.6		55.8		35.9	

experimental martensitic steel, the secondary cracks in the regions near the fracture surface of the N1 steel were carefully examined via both SEM-ECCI and HAR-EBSD.

Fig. 8a–c show the HAR-EBSD results for the crack, and the corresponding ECCI images of local regions (indicated by white frames and blue frames in Fig. 8c) are presented in Fig. 8d and e. As shown in Fig. 8d, a mixed feature of IG and TG cracking was observed. The crack propagated along the PAG boundaries in most regions. However, in the regions near the triple-points of the PAG, it propagated inside the PAG. Notably, the fragmentation and distortion of the martensite laths were observed near the triple-point regions (marked by white boxes in Fig. 8a and red boxes in Fig. 8d), indicating that these localized regions underwent a significant plastic-deformation process. To confirm this, the KAM map based on the calculation of the average misorientation between one pixel and its nearest neighbor pixels, which is commonly used to evaluate the localized dislocation density [63], was obtained, as shown in Fig. 8b. Higher KAM values were observed in the regions marked by the white box, indicating that the propagation of hydrogen-assisted cracks in the experimental steels was accompanied by

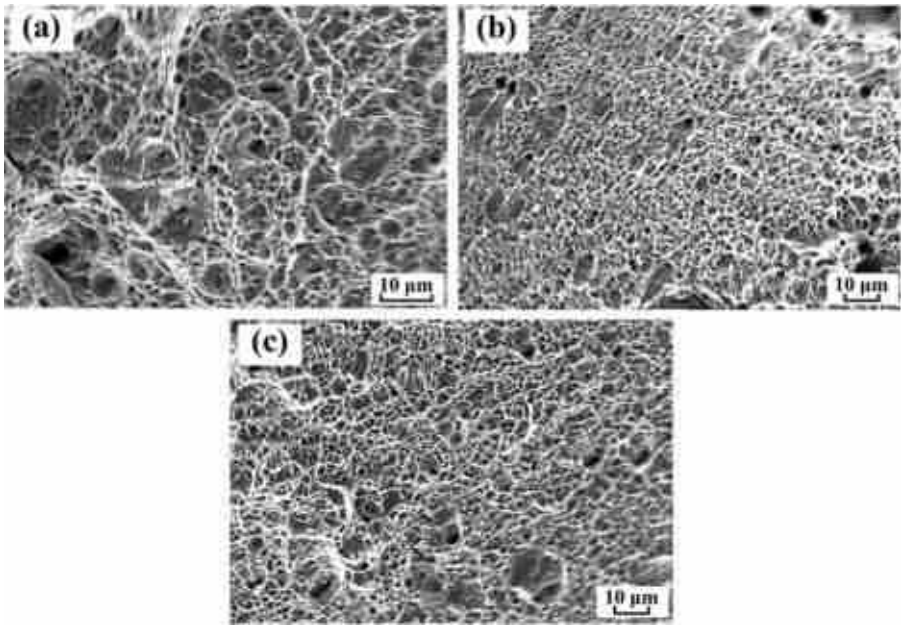

Fig. 6. SEM images of the fracture surfaces of hydrogen-uncharged specimens: (a) N1 steel, (b) N2 steel, and (c) N3 steel.

dislocation multiplication and movement in the local regions. Thus, the HELP mechanism was one of the HE mechanisms in the experimental steels. Moreover, according to the orientation data, a slip trace analysis was performed (shown in Fig. 8b), indicating that the crack propagated along the {110} planes. Okada et al. [64] proposed that {110} planes are slip planes of bcc steels and that the cracks propagating along {110} planes can arise from hydrogen-enhanced local slips on {110} planes. In the present study, the crack propagation along the {110} planes indicated that the HELP process occurred during the HE of the experimental steels.

Additionally, a branch crack that propagated along the martensite lath boundaries (Fig. 8d) was observed adjacent to the secondary crack, indicating that during the crack propagation, hydrogen accumulated at not only the PAG boundaries but also the martensite lath boundaries. It is generally believed that the local hydrogen concentration at such boundaries reduces the cohesive energy through the HEDE mechanism, resulting in boundary cracking [13,59]. Because the HEDE process did not introduce large plastic deformation, a high dislocation density was not observed near the crack. As shown in Fig. 8b, the dislocation density of the IG regions of the crack (indicated by red boxes) was not higher than that of the crack-free regions, confirming that HEDE was another mechanism of HE fracture in the experimental steel. According to the foregoing analysis, the HE process of the experimental steels was the joint effect of HELP and HEDE.

3.5. APT results

To directly investigate the influence of the NbC precipitates on the

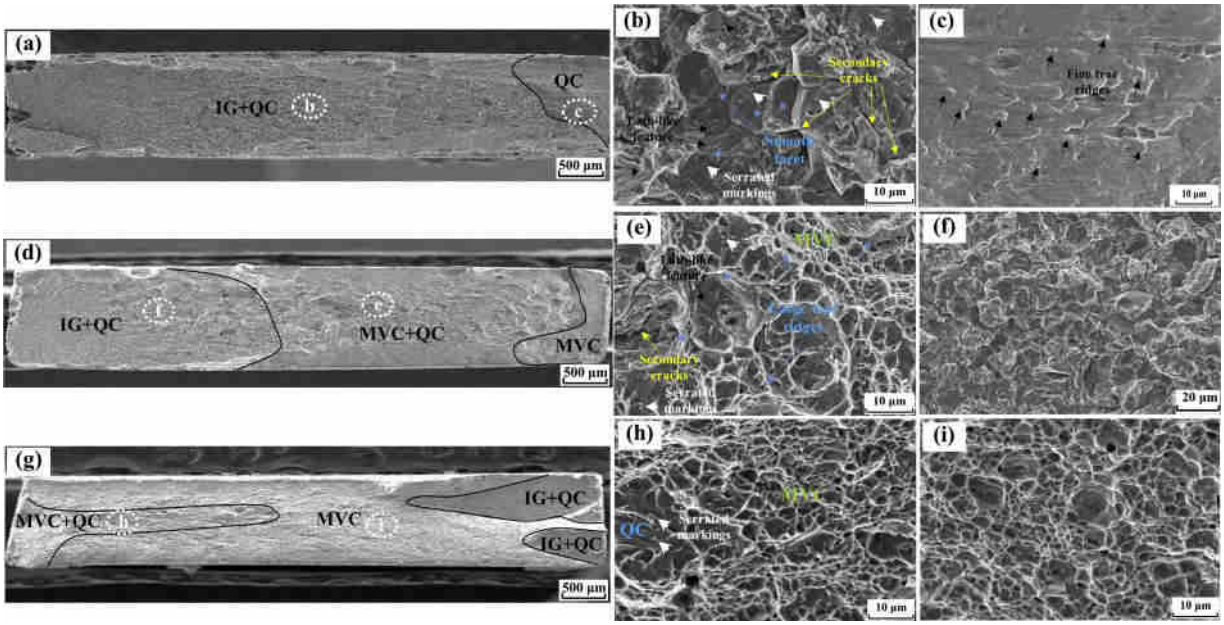

Fig. 7. SEM images of the fracture surfaces of hydrogen-charged specimens: (a) overview micrograph of N1, (b, c) enlargement of the fracture zone marked by the dashed line in (a); (d) overview micrograph of N2, (e, f) enlargement of the fracture zone marked by the dashed line in (d); (g) overview micrograph of N3, (h, i) enlargement of the fracture zone marked by the dashed line in (g).

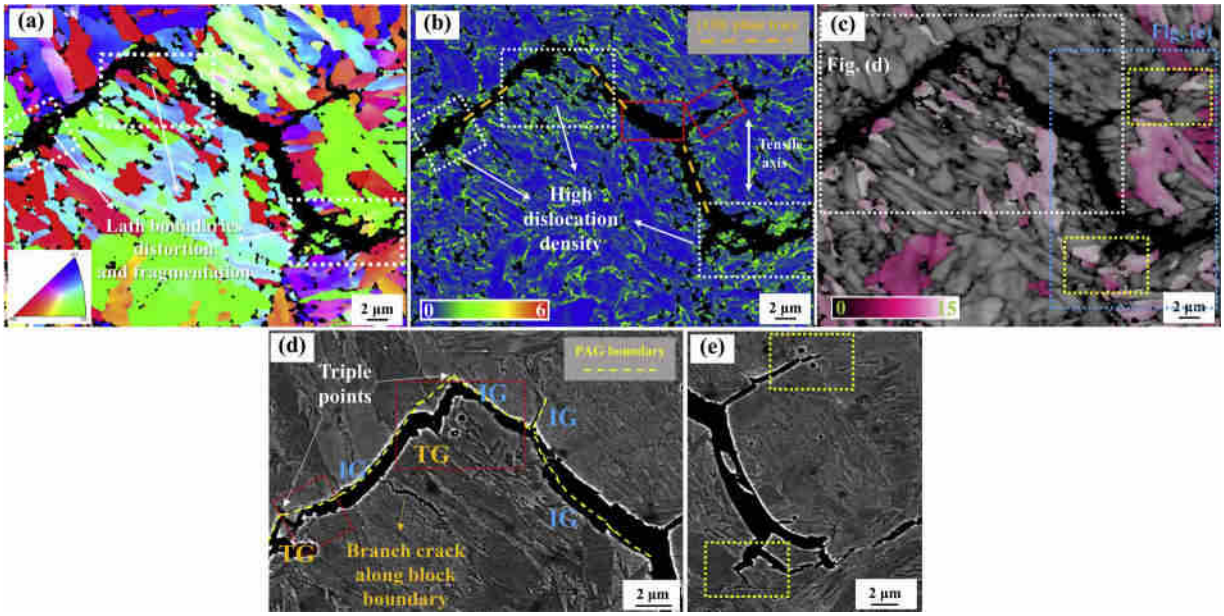

Fig. 8. HAR-EBSD results for the crack in the N1 steel: (a) inverse pole figure (IPF) map, (b) kernel average misorientation (KAM) map with {110} slip traces, and (c) {111}//ND texture map. (d, e) Corresponding ECCI images of local regions in (c).

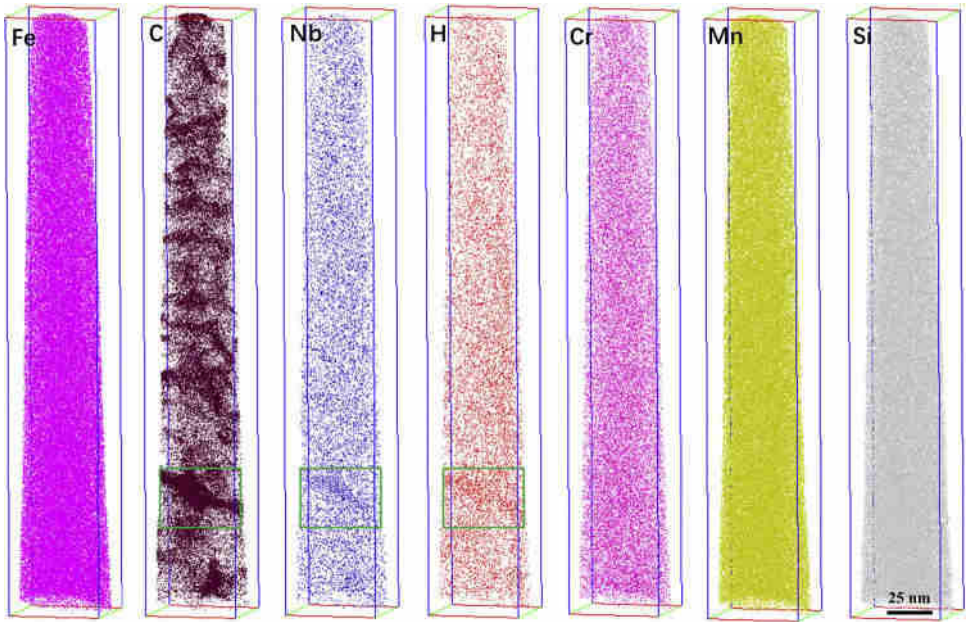

Fig. 9. 3D atom maps of H and the major alloy elements in the N3 steel.

hydrogen-trapping sites in the test steels, the atom distributions in the Nb-bearing N3 steel were mapped via APT. Fig. 9 shows the three-dimensional (3D) atom maps of H and the major alloy elements in the N3 steel. C, Nb, and H atoms were ununiformly distributed in the steel matrix, and the other elements exhibited no atom segregation. The enrichment of C, Nb, and H atoms in the same region (marked by a green box) was observed, indicating that the NbC precipitate existed in this local region. To highlight the NbC precipitate and the H distribution, the 7.4 at.% (C + Nb) isoconcentration surfaces of the green-box region were plotted in Fig. 10a, and the C, Nb, and H atoms inside the isoconcentration surfaces are shown in Fig. 10b. The precipitate size was approximately 25 nm, and a large number of hydrogen atoms were trapped by the precipitate, confirming that the NbC precipitate had a strong hydrogen-trapping ability. Note here, as mentioned in the introduction, the hydrogen concentration obtained by APT on hydrogen charged sample could not be used for quantitative analysis and only qualitative analysis is accepted. Similar qualitative analyses have already been successfully used in the previous literatures to prove that the reversed austenite, ε-carbide, and V enriched carbide are hydrogen trapping sites [3,46–49].

Moreover, as shown in Fig. 9, a pronounced heterogeneous distribution of C was observed in other regions, where the Nb and hydrogen were uniformly distributed. Previous APT studies on martensite revealed significant C segregation in the auto-tempered matrix after water quenching [65,66]. As illustrated in Fig. 9, the hydrogen segregation in the C-segregation regions was not obvious, indicating that the hydrogen-trapping ability of C segregation was insignificant.

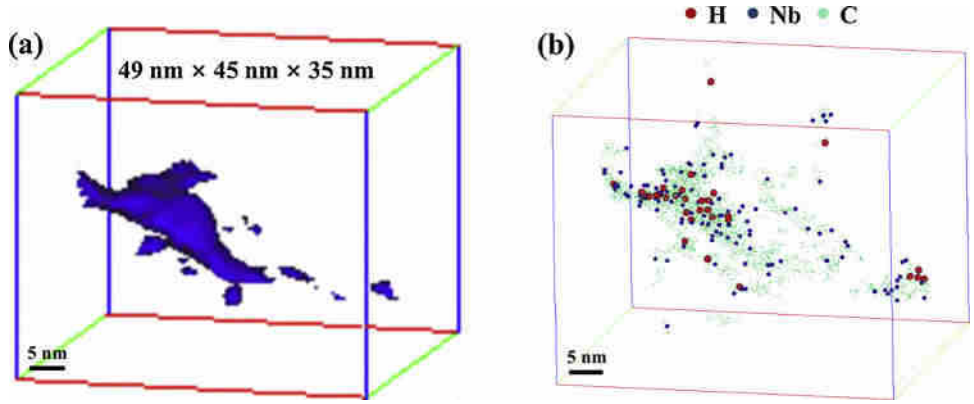

Fig. 10. (a) 7.4 at.% (C + Nb) isoconcentration surfaces of the green-box region in Fig. 9; (b) 3D view of the distributions of C, Nb, and H atoms inside the isoconcentration surfaces. (For interpretation of the references to colour in this figure legend, the reader is referred to the web version of this article).

3.6. Hydrogen permeation results and quantitative analysis

To evaluate the density of each type of hydrogen trap and the critical hydrogen concentration, hydrogen permeation tests were performed, and a quantitative model was established to analyse the results. Fig. 11 shows the hydrogen permeation curves for the three martensitic steels with different NbC amounts. According to the permeation curves and Eqs. (2)–(4), the permeation parameters were calculated, as shown in Table 3. A larger amount of NbC precipitate in the steel yielded a smaller D_{ap} and larger C_0. A smaller D_{ap} indicates that the hydrogen atoms had more difficulty diffusing through the steel and thus more difficulty aggregating in the defect sites, and a larger C_0 indicates a higher critical hydrogen concentration against cracking.

It is well established that D_{ap} and C_0 are determined by the external hydrogen-charging condition, as well as the hydrogen-trap states in the material. As the hydrogen-permeation conditions of the steels were the same in the permeation tests, the difference in the permeation coefficients is attributed to the difference in the hydrogen-trap states of the steels. Generally, according to the hydrogen-trapping energy, the hydrogen traps in steels can be classified into irreversible and reversible trap sites. The traps with a low trapping energy, such as lattice imperfections, grain boundaries, and dislocations, are regarded as reversible, and those with a high trapping energy, such as inclusions and precipitates, are considered as irreversible [39,60,67–69]. In the N1 steel, the hydrogen traps included grain boundaries (PAG boundaries, martensite packets, block and lath boundaries), dislocations, and inclusions. In the Nb-bearing steel, NbC precipitates also acted as irreversible hydrogen traps, and more grain-boundary traps were present

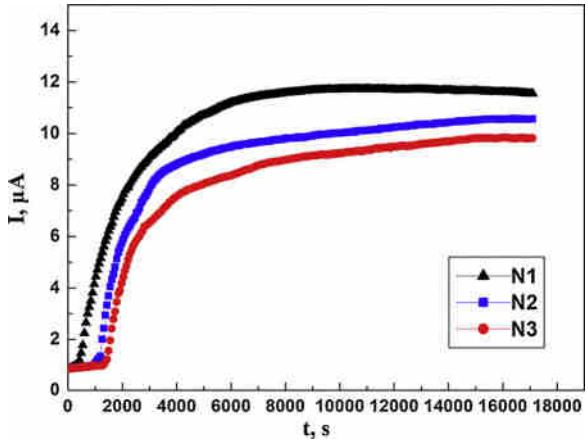

Fig. 11. Hydrogen permeation curves of the test steels with different NbC amounts.

Table 3
Permeation coefficients of the experimental steels.

Steel	N1	N2	N3
D_{ap}, 10^{-7} cm^2/s	8.938	8.033	6.352
C_0, 10^{-6} mol/cm^3	7.892	8.375	9.313

owing to the microstructure refinement due to the NbC. Thus, the total hydrogen-trap density (N_T) in the experimental steels can be determined by the following formula:

$$N_T = N_{GB} + N_{dis} + N_{pre} + N_{inc} + N_{other} \quad (5)$$

where N_{GB}, N_{dis}, N_{pre}, N_{inc}, and N_{other} represent the hydrogen-trap densities provided by grain boundaries, dislocations, NbC precipitates, inclusions, and other traps (such as solute atoms and vacancies), respectively.

In lath martensitic steel, a four-level hierarchy in the grain-boundary morphology, i.e. PAG boundaries, martensite packets, and block and lath boundaries, is observed. The hydrogen-trap density supplied by these grain boundaries can be evaluated as follows [70,71]:

$$N_{GB-k} = \frac{S_G x_{GB}}{2V_G x_a^3} = \frac{30}{d_k x_a^2} \quad (6)$$

$$N_{GB} = N_{GB\text{-}PAG} + N_{GB\text{-}MP} + N_{GB\text{-}MB} + N_{GB\text{-}ML} \quad (7)$$

Where, $N_{GB\text{-}k}$ (k = PAG/MP/MB/ML) represents the hydrogen-trap density provided by the PAG boundaries, martensite packet boundaries, martensite block boundaries, and martensite lath boundaries, respectively; S_G and V_G represent the surface area and volume, respectively, of the PAG or martensite packet/block/lath units (as the boundaries are shared by two units, the factor of 1/2 is selected here); x_a represents the atomic distance; x_{GB} represents the width of the boundary (approximately $10x_a$); and d_k (k = PAG/MP/MB/ML) represents the average size of PAG/martensite packet/block/lath units.

Additionally, the hydrogen-trap density provided by dislocations can be estimated as follows [71]:

$$N_{dis} = \frac{5\rho_{dis}}{x_a} \quad (8)$$

Where, 5 is the ratio of the dislocation width to the atomic distance, and ρ represents the dislocation density.

Furthermore, according to the hydrogen permeation results, N_T can be determined using the following equation [54,69]:

$$N_T = N_L \times \left(\frac{D_L}{D_{ap}} - 1\right) \times e^{-\left(E_b/RT\right)} \quad (9)$$

Where, $D_L = 1.28 \times 10^{-4}$ cm^2 s^{-1}, $N_L = 7.52 \times 10^{22}$ cm^{-3}, $E_b = 0.3$ eV,

Table 4
Measured average sizes for the substructures and the calculated dislocation densities for the experimental steels.

Steel	d_{PAG}, μm	d_{MP}, μm	d_{MB}, μm	d_{ML}, μm	ρ, 10^{14} m^{-2}
N1	17.45	4.73	1.25	0.324	9.36
N2	9.28	3.44	0.83	0.165	9.37
N3	6.97	2.78	0.76	0.136	9.42

Notes: d_{PAG}, d_{MP}, d_{MB}, and d_{ML} represent the average sizes of the PAG, martensite packet unit, martensite block unit, and martensite lath unit, respectively.

$R = 8.3145\ J\ K^{-1}\ mol^{-1}$, and $T = 300\ K$ [54,69].

The average PAG sizes of the steels were identified using OM images, the martensite packet/block/lath sizes were determined using SEM images and EBSD results, and the dislocation densities were calculated using XRD data. The statistical results for these microstructural parameters are presented in Table 4. According to Eqs. (5)–(9) and these microstructural parameters, the N_T, N_{GB}, and N_{dis} were determined, whereas the N_{pre}, N_{inc}, and N_{other} remained unknown. As the test steels had similar compositions and were subjected to the same smelting, processing, and heat treatments, it is reasonable to assume that the N_{inc} and N_{other} were identical among the steels; thus, both N_{pre} and $N_{inc} + N_{other}$ could be determined for all the steels.

The calculated density values for each type of hydrogen trap are presented in Table 5. The trap density (N_{pre}) of the NbC precipitates was several (3–5) orders of magnitude higher than that of the other trap types in the Nb-bearing steels. Moreover, it is known that for the permeation test, when the oxidation current reaches a stable value, each hydrogen-trapping site traps one hydrogen atom in steels; therefore, the trapped hydrogen concentration for NbC precipitates is several orders of magnitude higher than those for the grain boundaries and dislocations. As the hydrogen-trapping energy of NbC (39–68 kJ/mol) [34,50] is higher than those for dislocations (20.6–37.6 kJ/mol) [27,51,60,72] and grain boundaries (17.2–47.4 kJ/mol) [27,60,72], the contribution of the NbC precipitates to the improvement of the HE resistance greatly exceeded the contributions of the other traps. Furthermore, the NbC precipitates in the steels significantly increased the trap density of the grain boundaries (PAG boundaries, martensite packets, and block and lath boundaries) by refining the martensite microstructure.

3.7. Crystallographic results near fracture surfaces

It is widely recognized that the HE properties of steels are closely related to their crystallographic characteristics [64,73,74]. To examine the influence of the NbC precipitates on the crystallographic characteristics and the corresponding HE fracture behavior, EBSD observations were performed on the cross sections below the fracture surfaces (the location is illustrated in Fig. 1) of the three experimental steels.

The IPF and orientation distribution function (ODF at φ2 = 45°) maps of the experimental steels are shown in Fig. 12. After the addition of NbC, the PAG, martensite packets, and blocks were remarkably refined, and the martensite microstructure was more homogeneous. As shown in ODF maps (Fig. 12d–f), the texture intensity of the tested martensitic steel was reduced after Nb microalloying. The N1 steel exhibited a strong (111) < 11 > texture, the N2 steel exhibited a weak (111) < 10 > texture, and almost no texture was observed for the N3 steel. Similar phenomenon of fine NbC precipitates decreased the intensity of {111} texture has also been observed in other study [75], and they proposed that during the grain growth stage, {111} grains in Nb-free steel grow rapidly with eating other grains compared with those in Nb-bearing steel due to growth of austenitized grain in Nb-bearing steel is strongly suppressed by the fine NbC precipitates. Numerous previous studies [73,74,76,77] have indicated that the {111}//ND texture is beneficial to the improvement of the hydrogen-induced cracking (HIC) resistance, because the {111}//ND oriented grains can rotate according to the orientation of the maximum shear stress and accumulate large plastic deformation, reducing the driving force of crack propagation. In the present study, as shown in the {111}//ND texture map (Fig. 8c), {111}//ND grains were observed in the crack-arrested region (yellow boxes in Fig. 8c), indicating that such grains hindered the crack propagation in the tested steels. Moreover, {110} planes are believed to be one group of the slip planes in bcc metal [64]. In the experimental steel, as shown in Fig. 8b, the fracture facets were nearly parallel to one of the {110} traces (the dotted yellow line), confirming that the hydrogen-assisted crack in the tested steel propagated along the {110} planes. Under tensile stress, the {110} planes of the {111}//ND oriented grains were far from the shear-stress direction; thus, the crack had more difficulty propagating in the N1 steel compared with the other steels. According to the foregoing analysis, the NbC weakened the beneficial {111}//ND texture of the martensitic steel and reduced the crack-propagation resistance.

Fig. 13 shows the grain-boundary distribution maps and the volume fractions of each boundary in the tested steels. The proportion of each grain boundary did not change significantly after NbC addition; the fraction of low-angle grain boundaries (LAGBs) ($2^\circ < \theta < 5^\circ$) increased slightly, while the fraction of high-angle grain boundaries (HAGBs) ($15^\circ < \theta < 62.8^\circ$) decreased slightly. This may be because during the martensitic transformation, the addition of NbC, which did not significantly change the K-S orientation relationship between the martensite variant and austenite, had little influence on the grain-boundary fraction. However, although the fractions of the boundaries changed slightly, the number and the total surface area of grain boundaries in the Nb-bearing steels increased significantly owing to the grain-refinement effect of NbC. Previous studies indicated that both LAGBs and grain refinement are beneficial to the HE resistance of steels [69,76,78,79]. Thus, for the tested steels, the significantly increased total surface area of the grain boundaries, compared with the slightly increased LAGB fraction, contributed more to the higher HE resistance in the steels with NbC.

Fig. 14 shows the reconstruction coincidence site lattice (CSL) boundary maps and the corresponding frequencies for the different steels. In all the steels, Σ3 boundaries accounted for the largest fraction of CSL boundaries. Compared with the Nb-free N1 steel, the steels with NbC exhibited lower Σ3 proportions. In previous studies [69,78,80], the Σ3 boundary was found to reduce the HIC resistance of bcc steels, as it did not result from real twinning and exhibited similar characteristics to HAGBs. Therefore, the NbC enhanced the HIC resistance of the martensitic steel by reducing the proportion of the Σ3 boundary. In addition to the Σ3 boundary, the Nb-bearing steels exhibited slight differences in the proportions of other boundaries, such as Σ11, Σ17b, and Σ25b. The Σ11 boundary was reported to be beneficial for improving the HIC resistance [81]. The effects of the Σ17b and Σ25b

Table 5
Calculated values for various hydrogen traps.

Steel	N_T, 10^{24} cm^{-3}	$N_{GB\text{-}PAG}$, 10^{19} cm^{-3}	$N_{GB\text{-}MP}$, 10^{20} cm^{-3}	$N_{GB\text{-}MB}$, 10^{20} cm^{-3}	$N_{GB\text{-}ML}$, 10^{21} cm^{-3}	N_ρ, 10^{19} cm^{-3}	N_{pre}, 10^{24} cm^{-3}
N1	10.693	2.543	9.382	3.550	1.370	1.800	0
N2	11.906	4.782	1.290	5.347	2.690	1.801	1.211
N3	15.078	6.367	1.596	5.839	3.263	1.811	4.383

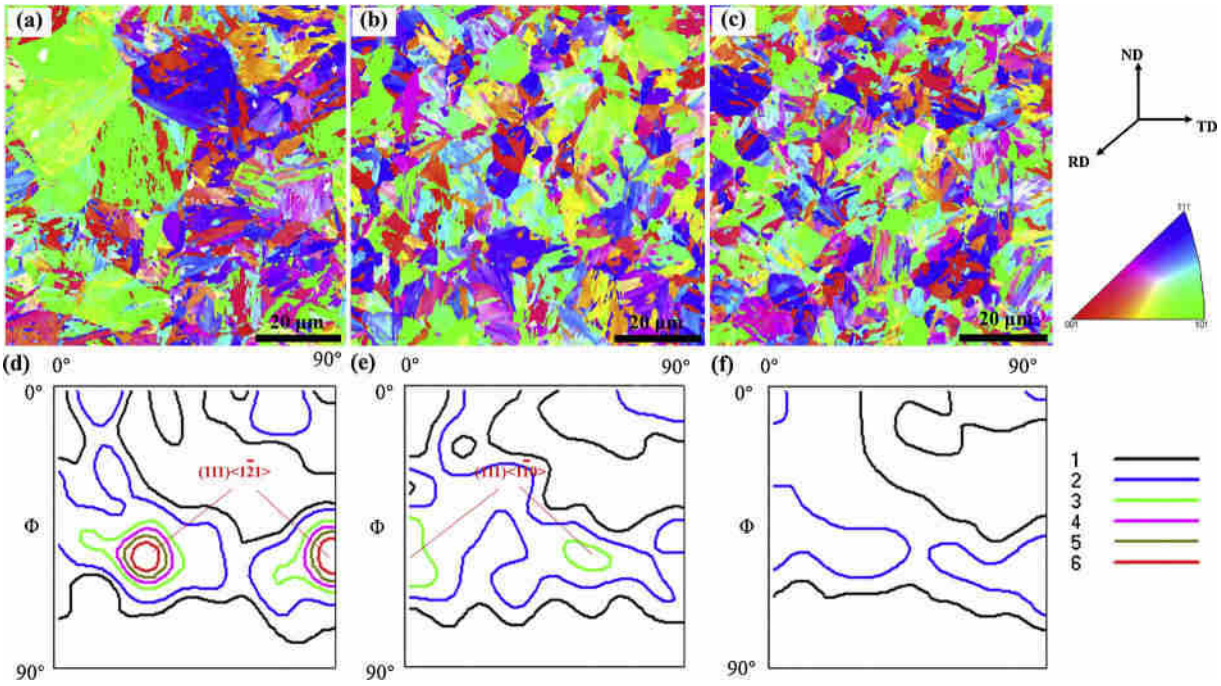

Fig. 12. IPF and ODF (φ2 = 45°) maps of the cross sections below the fracture surface in the (a) (d) N1 steel, (b) (e) N2 steel, and (c) (f) N3 steel. Note here to ensure the statistic of ODF maps, the ODF maps in (d–f) were obtained from large regions (not the small regions in a–c) which contain at least 800 grains.

boundaries on HIC are poorly understood. However, because the differences in the proportions of these boundaries were extremely small and their frequencies were significantly lower than that of Σ3, their influence can be ignored.

Fig. 15 shows the KAM distribution maps of regions around the fracture surfaces in the experimental steels and the corresponding relative-frequency curves. As shown in Fig. 15a–c, the martensite packet/block/lath boundaries in all the specimens exhibited higher KAM values than the matrix. The highest frequency of the KAM curve was around 0.95° for the N1 steel, while the value was approximately 0.7°–0.75° for

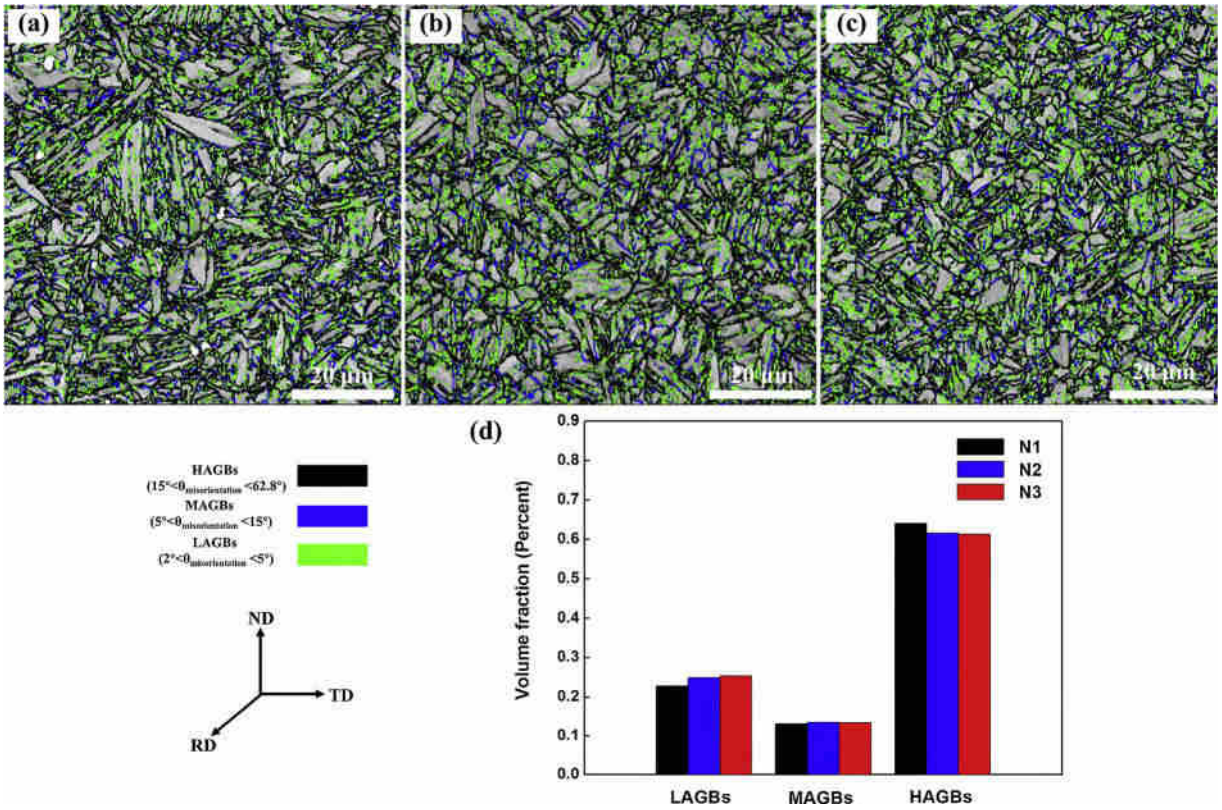

Fig. 13. Grain-boundary distribution maps of the cross sections below the fracture surface in the (a) N1 steel, (b) N2 steel, and (c) N3 steel, as well as (d) the volume fractions of each boundary.

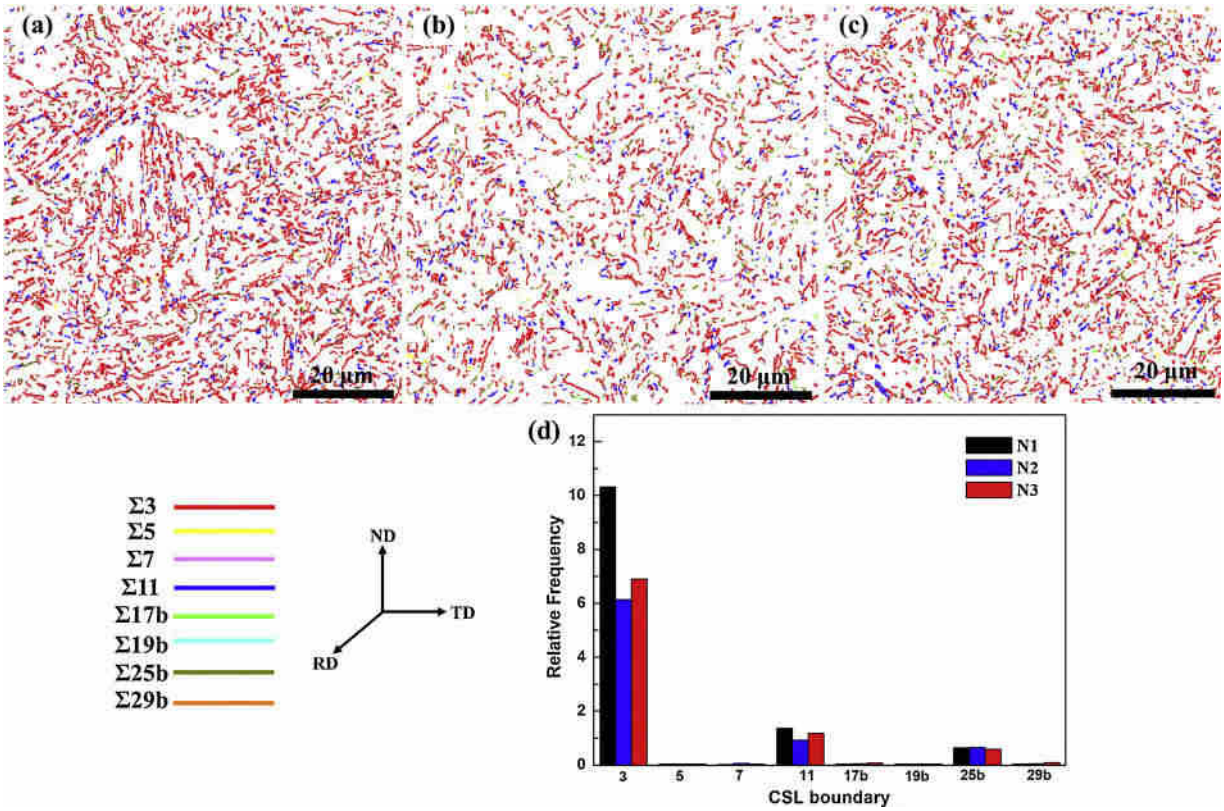

Fig. 14. CSL boundary maps of the cross sections below the fracture surface in the (a) N1 steel, (b) N2 steel, and (c) N3 steel, as well as (d) the frequency of each CSL boundary.

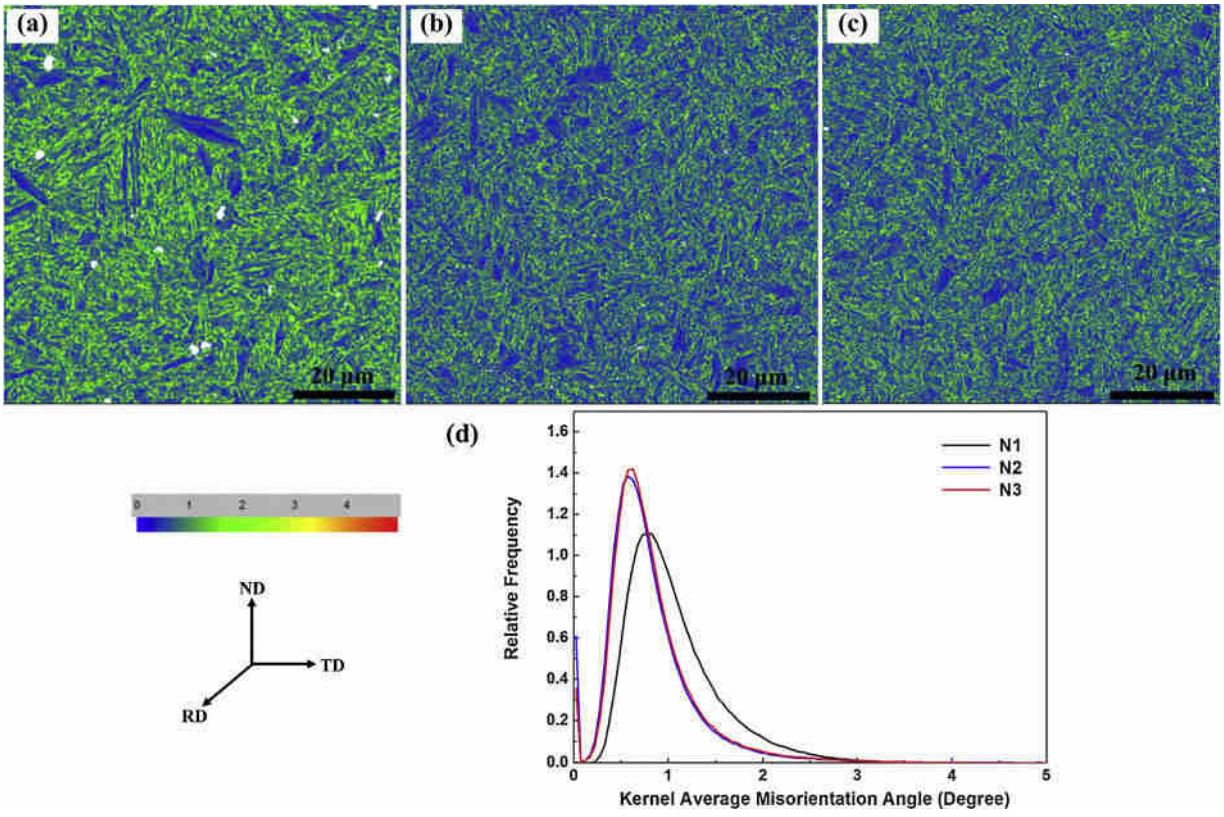

Fig. 15. KAM maps of the cross sections below the fracture surface in the (a) N1 steel, (b) N2 steel, and (c) N3 steel, as well as (d) the frequencies of the KAM values.

the Nb-bearing steels. Moreover, the Nb-bearing steels had lower average KAM values, indicating that the dislocation density in the region around the fracture surfaces of the hydrogen-charged specimens with NbC was lower than that for the N1 steel. In contrast, the XRD results for the undeformed experimental steels indicated that the Nb-bearing steels had a slightly higher dislocation density than the N1 steel. As shown in Fig. 8b, during HE fracture, the dislocation density of the steels was increased by the HELP mechanism. Thus, the dislocation-density increments resulting from HELP in the Nb-bearing steels were smaller than those in the Nb-free steel; i.e. the NbC precipitates hindered the HELP process. In HELP, the hydrogen atoms can interact with dislocations, leading to the formation of hydrogen-dislocation Cottrell atmospheres and the promotion of dislocation mobility and emission. Moreover, previous studies indicated that nanosized carbides (such as VC and NbC) can directly pin dislocations [82] and the corresponding hydrogen-dislocation atmospheres [83], which was confirmed by the TEM images obtained in the present study (Fig. 4f). When the movable hydrogen-dislocation Cottrell atmospheres are pinned by NbC precipitates during HE failure, hydrogen atoms are removed from dislocations and trapped by the carbides [83,84]; therefore, the movement and multiplication of dislocations are hindered, i.e. the HELP is inhibited.

3.8. Mechanisms of NbC precipitates on HE

The HE resistance of steel is mainly determined by its hydrogen trap status and microstructure characteristics. Here, the effects of the NbC precipitates on these two aspects and their consequent impact on the HE behavior are discussed. A schematic of the effects of the NbC precipitates on the HE in martensitic steel is shown in Fig. 16.

The effect of the NbC precipitates on the hydrogen trap status in the experimental steel involved the following two aspects. (i) As directly proven by the APT results (Figs. 9 and 10) and the quantitative analysis results of hydrogen traps in Section 3.6, the NbC precipitates were strong hydrogen-trapping sites and trapped large amounts of hydrogen. Previous studies [20,21] revealed that the precondition for the activation of the HEDE mechanism is that the local hydrogen concentration on defects (such as PAG boundaries in martensitic steel) is high enough and exceeds the critical hydrogen concentration. Thus, the presence of NbC precipitates homogenizes the hydrogen distribution, inhibits the enrichment of hydrogen at the PAG boundaries, and finally hinders the HEDE processes. (ii) The microstructure and quantitative analyses indicated that the NbC precipitates significantly refined and homogenized the martensite matrix, increasing the effective area of the PAG boundaries and packet/block/lath martensite boundaries. Thus, they provided additional reversible hydrogen traps, homogenizing the hydrogen distribution and suppressing the HEDE. Moreover, quantitative analysis indicated that the trapped hydrogen concentration of the NbC precipitates was several orders of magnitude higher than those of the other types of traps in the Nb-bearing steels, suggesting that the contribution of the NbC precipitates to suppressing the HEDE greatly exceeded the contributions of the other traps.

The effect of the NbC precipitates on the microstructure characteristics (crystallographic characteristics and dislocations) and the corresponding influence on the HE were as follows. (i) The NbC precipitates weakened the beneficial {111}//ND texture (Fig. 12); consequently, the hydrogen-assisted cracks propagated more easily, and the HELP was promoted in the experimental steels, increasing the HE susceptibility. Thus, the precipitates played a harmful role. (ii) The NbC precipitates reduced the Σ3 boundary fraction (Fig. 14) and increased the fraction of LAGBs in the steel (Fig. 13), increasing the hydrogen-induced crack-propagation resistance of the test martensitic steel and inhibiting the HELP. (iii) The NbC precipitates directly pinned hydrogen-dislocation Cottrell atmospheres and captured hydrogen from the atmospheres; thus, the dislocation movement and multiplication were hindered, and the HELP was weakened (KAM maps in Fig. 15). According to the foregoing analysis, the NbC precipitates played dual roles in influencing the HE behaviour of the martensitic steel. Their benefits far outweighed their disadvantages, and they ultimately improved the HE resistance.

4. Conclusion

1 The HE process of the experimental lath martensitic steels involved synergistic effects of the HELP and HEDE mechanisms.
2 Nanosized NbC precipitates reduced the HE susceptibility of the martensitic steels, and the susceptibility decreased with the increasing amount of NbC precipitates.
3 The nanosized NbC precipitates played dual roles in affecting the HE process of the lath martensitic steels, and the beneficial effects far outweighed the harmful effects.
4 Among the beneficial effects, the nanosized NbC precipitates increased the amount of irreversible and reversible hydrogen traps by providing NbC-induced traps and additional PAG/martensite boundary-induced traps. Consequently, the hydrogen accumulation in the local region was inhibited, and the HEDE was suppressed. Additionally, the NbC precipitates reduced the fraction of the Σ3

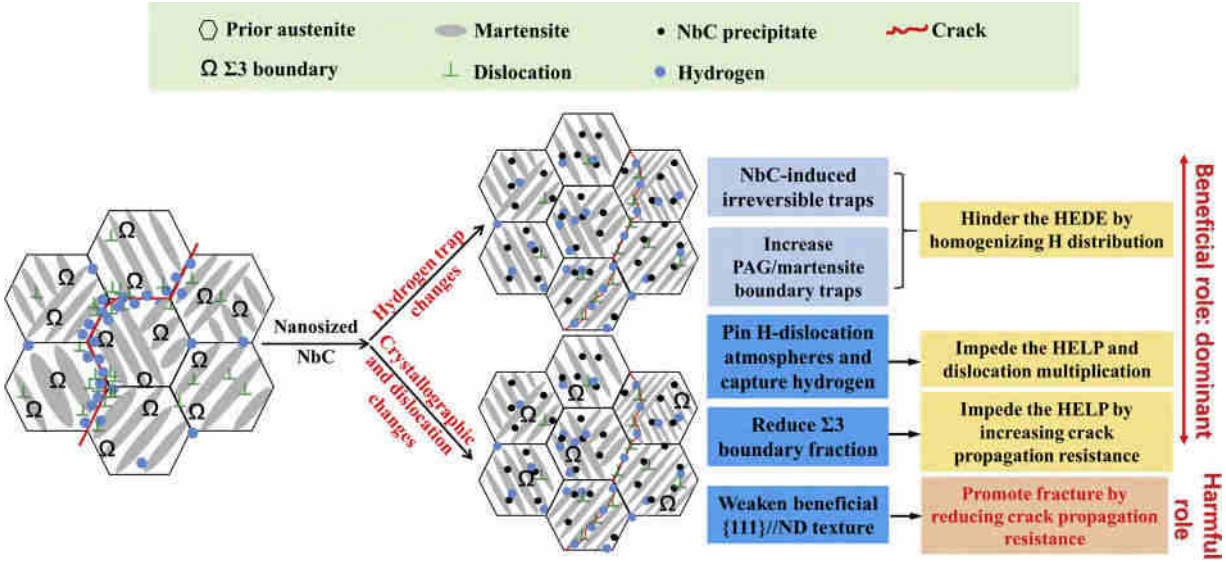

Fig. 16. Schematic illustrating the effects of the NbC precipitates on the HE in the martensitic steel.

boundary, which—combined with the pinning effect of NbC on the movable hydrogen-dislocation Cottrell atmospheres—inhibited the HELP.

5 The harmful role was that the nanosized NbC precipitates weakened the beneficial {111}//ND texture and thus promoted hydrogen-assisted fracture by reducing the crack-propagation resistance.

Declaration of Competing Interest

The authors declare that they have no known competing financial interests or personal relationships that could have appeared to influence the work reported in this paper.

Acknowledgments

This research was financially supported by the National Key Research and Development Program of China (No. 2016YFB0300604), the National Natural Science Foundation of China (Nos. 51971033, 51801011), the National Basic Research Program of China (No. 2014CB643300), and the National Materials Corrosion and Protection Data Center.

References

[1] X. Li, J. Zhang, E. Akiyama, Q. Li, Y. Wang, Effect of heat treatment on hydrogen-assisted fracture behavior of PH13-8Mo steel, Corros. Sci. 128 (2017) 198–212.
[2] S. Li, Z. Zhang, E. Akiyama, K. Tsuzaki, B. Zhang, Evaluation of susceptibility of high strength steels to delayed fracture by using cyclic corrosion test and slow strain rate test, Corros. Sci. 52 (5) (2010) 1660–1667.
[3] X. Zhu, W. Li, H. Zhao, L. Wang, X. Jin, Hydrogen trapping sites and hydrogen-induced cracking in high strength quenching & partitioning (Q&P) treated steel, Int. J. Hydrog. Energy 39 (2014) 13031–13040.
[4] J. Venezuela, J. Blanch, A. Zulkiply, Q. Liu, Q. Zhou, M. Zhang, A. Atrens, Further study of the hydrogen embrittlement of martensitic advanced high-strength steel in simulated auto service conditions, Corros. Sci. 135 (2018) 120–135.
[5] D. Figueroa, M.J. Robinson, Hydrogen transport and embrittlement in 300 M and AerMet100 ultra high strength steels, Corros. Sci. 52 (2010) 1593–1602.
[6] G. Wang, Y. Yan, J. Li, J. Huang, Y. Su, L. Qiao, Hydrogen embrittlement assessment of ultra-high strength steel 30CrMnSiNi2, Corros. Sci. 77 (2013) 273–280.
[7] M.R. Louthan Jr, Hydrogen embrittlement of metals: a primer for the failure analyst, J. Fail, Anal. and Preven. 8 (2008) 289–307.
[8] I.M. Robertson, P. Sofronis, A. Nagao, M.L. Martin, S. Wang, D.W. Gross, K.E. Nygren, Hydrogen embrittlement understood, Metall. Mater. Trans. A 26 (2015) 2323–2341.
[9] L. Cho, D.H. Sulistiyo, E.J. Seo, K.R. Jo, S.W. Kim, J.K. Oh, Y.R. Cho, B.C. De Cooman, Hydrogen absorption and embrittlement of ultra-high strength aluminized press hardening steel, Mater. Sci. Eng. A 734 (2018) 416–426.
[10] D. Hardie, E.A. Charles, A.H. Lopez, Hydrogen embrittlement of high strength pipeline steels, Corros. Sci. 48 (12) (2006) 4378–4385.
[11] Q. Liu, Q. Zhou, J. Venezuela, M. Zhang, A. Atrens, Hydrogen influence on some advanced high-strength steels, Corros. Sci. 125 (2017) 114–138.
[12] C. Zapffe, C. Sims, Hydrogen embrittlement, internal stress and defects in steel, Trans. AIME 145 (1941) 225–271.
[13] A.R. Troiano, The role of hydrogen and other interstitials in the mechanical behavior of metals, Trans. ASM 52 (1960) 54–80.
[14] R.A. Oriani, A mechanistic theory of hydrogen embrittlement of steels, Ber. Bunsenges. Phys. Chem. (1972) 848–857.
[15] M. Nagumo, Hydrogen related failure of steels – a new aspect, Mater. Sci. Technol. 20 (2004) 940–950.
[16] H.K. Birnbaum, P. Sofronis, Hydrogen-enhanced localized plasticity—a mechanism for hydrogen-related fracture, Mater. Sci. Eng. A 176 (1994) 191–202.
[17] I.M. Robertson, The effect of hydrogen on dislocation dynamics, Eng. Fract. Mech. 68 (6) (2001) 671–692.
[18] S.P. Lynch, Environmentally assisted cracking: overview of evidence for an adsorption-induced localised-slip process, Acta Metall. 36 (1988) 2639–2661.
[19] P. Novak, R. Yuan, B.P. Somerday, P. Sofronis, R.O. Ritchie, A statistical, physical-based, micro-mechanical model of hydrogen-induced intergranular fracture in steel, J. Mech. Phys. Solids 58 (2010) 206–226.
[20] X. Li, J. Zhang, E. Akiyama, Y. Wang, Q. Li, Microstructural and crystallographic study of hydrogen-assisted cracking in high strength PSB1080 steel, Int. J. Hydrog. Energy 43 (2018) 17898–17911.
[21] M. Djukic, V.S. Zeravcic, G. Bakic, A. Sedmak, B. Rajicic, Hydrogen damage of steels: a case study and hydrogen embrittlement model, Eng. Fail. Anal. 58 (2015) 485–498.
[22] M. Garet, A.M. Brass, C. Haut, F. Guttierez-Solana, Hydrogen trapping on non metallic inclusions in cr-mo low alloy steels, Corros. Sci. 40 (1998) 1073–1086.
[23] T. Michler, Y. Lee, R.P. Gangloff, J. Naumann, Influence of macro segregation on hydrogen environment embrittlement of SUS 316L stainless steel, Int. J. Hydrogen Energy 34 (2009) 3201–3209.
[24] Y.J. Kwon, H.J. Seo, J.N. Kim, C.S. Lee, Effect of grain boundary engineering on hydrogen embrittlement in Fe-Mn-C TWIP steel at various strain rates, Corros. Sci. 142 (2018) 213–221.
[25] B. Szost, R. Vegter, P. Rivera-Díaz-del-Castillo, Developing bearing steels combining hydrogen resistance and improved hardness, Mater. Des. 43 (2013) 499–506.
[26] T. Michler, M.P. Balogh, Hydrogen environment embrittlement of an ODS RAF steel–Role of irreversible hydrogen trap sites, Int. J. Hydrogen Energy 35 (18) (2010) 9746–9754.
[27] J. Zhao, Z. Jiang, C.S. Lee, Effects of tungsten on the hydrogen embrittlement behaviour of microalloyed steels, Corros. Sci. 82 (2014) 380–391.
[28] H. Noh, J. Kang, K. Kim, S. Kim, The effect of carbon on hydrogen embrittlement in stable Cr-Ni-Mn-N austenitic stainless steels, Corros. Sci. 124 (2017) 63–70.
[29] T. Depover, K. Verbeken, Evaluation of the effect of V4C3 precipitates on the hydrogen induced mechanical degradation in Fe-C-V alloys, Mater. Sci. Eng. A 675 (2016) 299–313.
[30] H.J. Kim, S.H. Jeon, W.S. Yang, B.G. Yoo, Y.D. Chung, H.Y. Ha, H.Y. Chung, Effects of titanium content on hydrogen embrittlement susceptibility of hot-stamped boron steels, J. Alloy. Comp. 735 (2018) 2067–2080.
[31] T. Depover, K. Verbeken, The effect of TiC on the hydrogen induced ductility loss and trapping behavior of Fe-C-Ti alloys, Corros. Sci. 112 (2016) 308–326.
[32] J. Lee, T. Lee, Y.J. Kwon, D. Mun, J. Yoo, C.L. Lee, Effects of vanadium carbides on hydrogen embrittlement of tempered martensitic steel, Met. Mater. Int. 22 (2016) 364–372.
[33] L. Cho, E.J. Seo, D.H. Sulistiyo, K.R. Jo, S.W. Kim, J.K. Oh, Y.R. Cho, B.C.D. Cooman, Influence of vanadium on the hydrogen embrittlement of aluminized ultra-high strength press hardening steel, Mater. Sci. Eng. A 735 (2018) 448.
[34] S.Q. Zhang, Y.H. Huang, B.T. Sun, Q.L. Liao, H.Z. Lu, B. Jian, Effect of Nb on hydrogen-induced delayed fracture in high strength hot stamping steels, Mater. Sci. Eng. A 626 (2015) 136–143.
[35] L. Lin, B. Li, G. Zhu, Y. Kang, R. Liu, Effect of niobium precipitation behavior on microstructure and hydrogen induced cracking of press hardening steel 22MnB5, Mater. Sci. Eng. A 721 (2018) 38–46.
[36] M.A. Mohtadi-Bonab, M. Eskandari, A focus on different factors affecting hydrogen induced cracking in oil and natural gas pipeline steel, Eng. Fail. Anal. 79 (2017) 351–360.
[37] M.A. Mohtadi-Bonab, M. Eskandari, J.A. Szpunar, Effect of arisen dislocation density and texture components during cold rolling and annealing treatments on hydrogen induced cracking susceptibility in pipeline steel, J. Mater. Res. 31 (2016) 3390–3400.
[38] M.A. Mohtadi-Bonab, R. Karimdadashi, M. Eskandari, J.A. Szpunar, Hydrogen-induced cracking assessment in pipeline steels through permeation and crystallographic texture measurements, J. Mater. Eng. Perform. 25 (2016) 1781–1793.
[39] F.G. Wei, K. Tsuzaki, Hydrogen trapping phenomena in martensitic steels, Gaseous HE of materials in energy technologies, Woodhead (2012) 493–525.
[40] F.G. Wei, K. Tsuzaki, Quantitative Analysis on hydrogen trapping of TiC particles in steel, Metall. Mater. Trans. A 37A (2006) 331–353.
[41] F.G. Wei, T. Hara, K. Tsuzaki, Nano-precipitates design with hydrogen trapping character in high strength steels, Proceedings of the 2008 International Hydrogen Conference, Grand Teton National Park, WY, USA, 2009.
[42] A. Turk, D.S. Martin, P.E.J. Rivera-Diaz-del-Castillo, E.I. Galindo-Nava, Correlation between vanadium carbide size and hydrogen trapping in ferritic steel, Scripta Mater. 152 (2018) 112–116.
[43] J. Takahashi, K. Kawakami, Y. Kobayashi, Origin of hydrogen trapping site in vanadium carbide precipitation strengthening steel, Acta Mater. 153 (2018) 193–204.
[44] J. Takahashi, K. Kawakami, Y. Kobayashi, T. Tarui, The first direct observation of hydrogen trapping sites in TiC precipitation-hardening steel through atom probe tomography, Scripta Mater. 63 (2010) 261–264.
[45] Y.S. Chen, D. Haley, S.S.A. Gerstl, A.J. London, F. Sweeney, R.A. Wepf, W.M. Rainforth, P.A.J. Bagot, M.P. Moody, Direct observation of individual hydrogen atoms at trapping sites in a ferritic steel, Science 355 (6330) (2017) 1196–1199.
[46] Y. Fan, B. Zhang, H. Yi, G. Hao, Y. Sun, J. Wang, E.-H. Han, W. Ke, The role of reversed austenite in hydrogen embrittlement fracture of S41500 martensitic stainless steel, Acta Mater. 139 (2017) 188–195.
[47] X. Cheng, Z. Zhang, W. Liu, X. Wang, Direct observation of hydrogen-trapping sites in newly developed high-strength mooring chain steel by atom probe tomography, Prog. Nat. Sci.: Mater. Int. 23 (2013) 446–452.
[48] X.Y. Cheng, H. Li, X.B. Cheng, Carbides and possible hydrogen irreversible trapping sites in ultrahigh strength round steel, Micron 103 (2017) 22–28.
[49] X.B. Cheng, X.Y. Cheng, C.W. Jiang, X.Y. Zhang, Q.F. Wen, Hydrogen diffusion and trapping in V-microalloyed mooring chain steels, Mater. Lett. 213 (2018) 118–121.
[50] E. Wallaert, T. Depover, M.A. Arafin, K. Verbeken, Thermal desorption spectroscopy evaluation of the hydrogen trapping capacity of NbC and NbN precipitates, Metall. Mater. Trans. A 45 (2014) 2412–2420.
[51] M. Stopher, P. Lang, E. Kozeschnik, P. Rivera-Diaz-del-Castillo, Modelling hydrogen migration and trapping in steels, Mater. Des. 106 (2016) 205–215.
[52] T. Ungár, A. Borbély, The effect of dislocation contrast on x-ray line broadening: a new approach to line profile analysis, Appl. Phys. Lett. 69 (1996) 3173–3175.
[53] M.A.V. Devanathan, Z. Stachurski, The mechanism of hydrogen evolution on iron in acid solutions by determination of permeation rates, J. Electrochem. Soc. 111 (1964) 619–623.
[54] C.F. Dong, Z.Y. Liu, X.G. Li, Y.F. Cheng, Effects of hydrogen-charging on the susceptibility of X100 pipeline steel to hydrogen-induced cracking, Int. J. Hydrogen Energy 34 (2009) 9879–9884.
[55] S.K. Yen, I.B. Huang, Critical hydrogen concentration for hydrogen-induced

blistering on AISI 430 stainless steel, Mater. Chem. Phys. 80 (2003) 662–666.
[56] P. Gong, E.J. Palmiere, W.M. Rainforth, Dissolution and precipitation behaviour in steels microalloyed with niobium during thermomechanical processing, Acta Mater. 97 (2015) 392–403.
[57] T. Gladman, Precipitation hardening in metals, Mater. Sci. Technol. 15 (1) (1999) 30–36.
[58] B.S. Kumar, V. Kain, M. Singh, B. Vishwanadh, Influence of hydrogen on mechanical properties and fracture of tempered 13 wt% Cr martensitic stainless steel, Mater. Sci. Eng. A 700 (2017) 140–151.
[59] A. Nagao, C.D. Smith, M. Dadfarnia, P. Sofronis, I.M. Robertson, The role of hydrogen in hydrogen embrittlement fracture of lath martensitic steel, Acta Mater. 60 (2012) 5182–5189.
[60] A. Nagao, M. Dadfarnia, B.P. Somerday, P. Sofronis, R.O. Ritchie, Hydrogen-enhanced-plasticity mediated decohesion for hydrogen-induced intergranular and quasi-cleavage fracture of lath martensitic steels, J Mech Phys Solid 112 (2018) 403–430.
[61] M. Koyama, C.C. Tasan, E. Akiyama, K. Tsuzaki, D. Raabe, Hydrogen-assisted decohesion and localized plasticity in dual-phase steel, Acta Mater. 70 (2014) 174–187.
[62] M. Djukic, V.S. Zeravcic, G. Bakic, A. Sedmak, B. Rajicic, Hydrogen embrittlement of low carbon structural steel, Procedia Mater. Sci. 3 (2014) 1167–1172.
[63] S.I. Wright, M.M. Nowell, D.P. Field, A review of strain analysis using Electron backscatter Diffraction, Microsc. Microanal. 17 (3) (2011) 14.
[64] K. Okada, A. Shibata, Y. Takeda, N. Tsuji, Crystallographic feature of hydrogen-related fracture in 2Mn-0.1C ferritic steel, Int. J. Hydrogen Energy 43 (2018) 11298–11306.
[65] L. Morsdorf, C.C. Tasan, D. Ponge, D. Raabe, 3D structural and atomic-scale analysis of lath martensite: effect of the transformation sequence, Acta Mater. 95 (2015) 366–377.
[66] B. Hutchinson, J. Hagstro, Microstructures and hardness of as-quenched martensites (0.1–0.5%C), Acta Mater. 59 (2011) 5845–5858.
[67] G.M. Pressouyre, A classification of hydrogen traps in steel, Metall. Trans. A 10 (1979) 1571–1573.
[68] P.C. Rivera, V.P. Ramunni, P. Bruzzoni, Hydrogen trapping in an API 5L X60, Corros. Sci. 54 (2012) 106–118.
[69] S.Q. Zhang, E.D. Fan, J.F. Wan, J. Liu, Y.H. Huang, X.G. Li, Effect of Nb on the hydrogen-induced cracking of high-strength low-alloy steel, Corros. Sci. 139 (2018) 83–96.
[70] Y. Liu, M. Wang, G. Liu, Hydrogen trapping in high strength martensitic steel after austenitized at different temperatures, Int. J. Hydrog. Energy 38 (2013) 14364–14368.
[71] Q. Wang, Y. Sun, S.J. Gu, Z.N. He, Q.F. Wang, F.C. Zhang, Effect of quenching temperature on sulfide stress cracking behavior of martensitic steel, Mater. Sci. Eng. A. 724 (2018) 131–141.
[72] W.Y. Choo, J.Y. Lee, Thermal analysis of trapped hydrogen in pure iron, Metall. Trans. A 13A (1982) 135–140.
[73] M. Masoumi, L.P.M. Santos, I.N. Bastos, S.S.M. Tavares, M.J.G. da Silva, H.F.G. de Abreu, Texture and grain boundary study in high strength Fe–18Ni–Co steel related to hydrogen embrittlement, Mater. Des. 91 (2016) 90–97.
[74] M. Béreš, L. Wu, L. Santos, M. Masoumi, F. da Rocha Filho, C. da Silva, H. de Abreu, M. da Silva, Role of lattice strain and texture in hydrogen embrittlement of 18Ni (300) maraging steel, Int. J. Hydrogen Energy 21 (2017) 14786–14793.
[75] S. Satoh, T. Obara, K. Tsunoyama, Effect of precipitate dispersion on recrystallization texture of niobium-added extra-low carbon cold-rolled steel sheet, Trans. Iron Steel Inst. Jpn. 26 (1986) 737–744.
[76] M. Masoumi, C.C. Silva, H.F.G. Abreu, Effect of crystallographic orientations on the hydrogen-induced cracking resistance improvement of API 5L X70 pipeline steel under various thermomechanical processing, Corros. Sci. 111 (2016) 121–131.
[77] V. Venegas, F. Caleyo, T. Baudin, J.H. Espina-hernández, J.M. Hallen, On the role of crystallographic texture in mitigating hydrogen-induced cracking in pipeline steels, Corros. Sci. 53 (2011) 4204–4212.
[78] M.A. Mohtadi-Bonab, M. Eskandari, J.A. Szpunar, Texture, local misorientation, grain boundary and recrystallization fraction in pipeline steels related to hydrogen induced cracking, Mater. Sci. Eng. A 620 (2015) 97–106.
[79] C. Park, N. Kang, S. Liu, Effect of grain size on the resistance to hydrogen embrittlement of API 2W Grade 60 steels using in situ slow-strain-rate testing, Corros. Sci. 128 (2017) 33–41.
[80] M.A. Arafin, J.A. Szpunar, A new understanding of intergranular stress corrosion cracking resistance of pipeline steel through grain boundary character and crystallographic texture studies, Corros. Sci. 51 (2009) 119–128.
[81] V. Venegas, F. Caleyo, T. Baudinb, J.M. Hallen, R. Penelle, Role of microtexture in the interaction and coalescence of hydrogen-induced cracks, Corros. Sci. 51 (2009) 1140–1145.
[82] S.B. Wang, X.F. Chang, J. Key, New insight into high-temperature creep deformation and fracture of T92 steel involving precipitates, dislocations and nanovoid, Mater. Charact. 127 (2017) 1–11.
[83] A. Nagao, M.L. Martin, M. Dadfarnia, P. Sofronis, M. Robertson, The effect of nanosized (Ti,Mo)C precipitates on hydrogen embrittlement of tempered lath martensitic steel, Acta Mater. 74 (2014) 244–254.
[84] L. Li, B. Song, Z. Cai, Z. Liu, X. Cui, Effect of vanadium content on hydrogen diffusion behaviors and hydrogen induced ductility loss of X80 pipeline steel, Mater. Sci. Eng. A 742 (2019) 712–721.